Available online at www.sciencedirect.com

ScienceDirect

Geochimica et Cosmochimica Acta 272 (2020) 276–286

Geochimica et Cosmochimica Acta

www.elsevier.com/locate/gca

Discovery of nanophase iron particles and high pressure clinoenstatite in a heavily shocked ordinary chondrite: Implications for the decomposition of pyroxene

Zhuang Guo [a,b,c], Yang Li [a,d,*], Shen Liu [b,*], Huifang Xu [e], Zhidong Xie [h], Shijie Li [a,d], Xiongyao Li [a,d], Yangting Lin [f], Ian M. Coulson [g], Mingming Zhang [a,d]

[a] Center for Lunar and Planetary Sciences, Institute of Geochemistry, Chinese Academy of Sciences, Guiyang 550081, China
[b] State Key Laboratory of Continental Dynamics and Department of Geology, Northwest University, Xi'an 710069, China
[c] University of Chinese Academy of Sciences, Beijing 100049, China
[d] Center for Excellence in Comparative Planetology, Chinese Academy of Sciences, China
[e] Department of Geoscience, University of Wisconsin-Madison, Madison, WI 53706-1692, USA
[f] Institute of Geology and Geophysics, Chinese Academy of Sciences, Beijing 100029, China
[g] Solid Earth Studies Laboratory, Department of Geology, University of Regina, Regina, Saskatchewan S4S 0A2, Canada
[h] School of Earth Sciences and Engineering, Nanjing University, Nanjing 210023, China

Received 7 July 2019; accepted in revised form 26 October 2019; Available online 4 November 2019

Abstract

Although pure metallic iron (i.e. that with an Fe content of greater than 99%) commonly occurs in achondrites, and within the returned soil from asteroids or the Lunar surface, it is rarely found in ordinary chondrites meteorites. Abundant nanophase iron particles (np-Fe^0) were identified in pyroxene glass, within the shock melt vein of Grove Mountains (GRV) 022115, which is an ordinary (L6) chondrite, with a shock stage determined as S5. The association of np-Fe^0, highly defective high pressure clinoenstatite (HP-CEn), silica glass, as well as vesicles, embedded in a pyroxene glass selvage within the shock melt vein in this meteorite suggests that these phases formed as the result of decomposition of the host pyroxene grain, a process induced by the shock event that affected GRV 022115. The reaction to account for this mineral breakdown can be written as: $FeSiO_3 \rightarrow Fe + SiO_2 + 1/2O_2 \uparrow$ ($MgSiO_3$ remain in the HP-CEn). The pressure and temperature condition attending this reaction are estimated at 20–23 GPa and over 1800 °C, as indicated by the surrounded high-pressure mineral assemblage: ringwoodite, majorite, and magnesiowüstite. This study provides evidence to the formation of np-Fe^0 derived from pyroxene, and HP-CEn quenched metastably in such shocked vein could preserve the metastable phase transitions history record.

Keywords: Ordinary chondrite; Pyroxene; High-pressure clinoenstatite; Pure metallic iron; Shock metamorphism

1. INTRODUCTION

The presence of shock-induced melt veins within the meteorite can provide invaluable insight to the nature and mechanisms of phase transformation under extreme pressure and temperature conditions that attend this form of metamorphism; such veins also provide material that may deepen our understanding of the processes and materials

* Corresponding authors at: Center for Lunar and Planetary Sciences, Institute of Geochemistry, Chinese Academy of Sciences, Guiyang 550081, China (Y. Li).
E-mail addresses: liyang@mail.gyig.ac.cn (Y. Li), liushen@nwu.edu.cn (S. Liu).

https://doi.org/10.1016/j.gca.2019.10.036
0016-7037/

found within the Earth's interior. High-pressure silicate mineral assemblages are very common to shock-induced melt veins of ordinary chondrites (Stöffler et al., 1991; Stoffler and Langenhorst, 1994), and these phase associations have proven an effective means of estimating the shock conditions encountered by their host meteorites and any related, impacted terrestrial rocks (Robertson et al., 1977; Xie et al., 2006b, 2006c; Pang et al., 2016).

Meteorites and soil samples returned from the Lunar and asteroid (e.g., Itokawa) surface have facilitated the study of native iron species, such as the presence of nanophase iron particles (np-Fe^0). Current research suggests that iron nanoparticles form through the reduction of fayalitic olivine (Boland and Duba, 1981; Leroux et al., 2000; Sasaki et al., 2001; Leroux et al., 2003; Noguchi et al., 2011), Postulated reduction reaction include: $Fe_2SiO_4 = 2Fe + SiO_2 + O_2$ or $Fe_2SiO_4 = Fe + FeSiO_3 + 1/2O_2\uparrow$, with the first reaction liberating both native Fe-metal and a high proportion of SiO_2 from the silicate phase (Palme et al., 1988; Benzerara et al., 2002; Warren et al., 2014). At the same time, the phenomenon of "dusty olivine" in chondritic meteorites has also been explained by presence of reduced iron particles, which provide a significant record of remanent pre-accretionary processes (Lappe et al., 2011; Leroux et al., 2003). Disproportionation of Fe^{2+} had been proved under Earth mantle conditions and the high-pressure phases have a sufficient capacity to incorporate Fe^{3+} (e.g. Silicate perovskite, ringwoodite), which had been used to explain the presence of metallic iron in NWA 2737 (Frost et al., 2004; van de Moortele et al., 2007; Bläß et al., 2010).

There are rare cases reported in the literature for the decomposition of pyroxene in natural meteoritic samples, but in contrast to olivine, this break down has not led to evident metallic iron. For example, symplectitic clasts that are typical textures found within HED meteorites, were suggested to have formed through the breakdown of metastable Fe-rich pyroxene (Barrat et al., 2012). Moreover, the reduction of orthopyroxene had been proposed in shock metamorphism affecting the Tatahounine meteorite, but without the evidence of Fe gradients (Benzerara et al., 2002). Tomioka and Fujino (1997) have suggested that the decomposition of pyroxene is difficult to complete in a shock event, because of the rapid cooling rate. Thus, whether or not pyroxene can decompose in the environment of space to contribute to the formation of iron nanoparticles is questionable.

High-pressure clinoenstatite (HP-CEn, the $MgSiO_3$ end-member of HP-Cpx) is an important monoclinic polymorph of low-Ca pyroxene (Angel et al., 1992; Akashi et al., 2009; Yoshiasa et al., 2013; Xu et al., 2017). Many simulation experiments have been carried out to study the (Mg, Fe) SiO_3 orthoenstatite (OEn) to high-pressure clinoenstatite (HP-CEn) transformation, and the low clinoenstatite (L-CEn) is commonly observed in the terrestrial samples and meteorites (Tomioka and Fujino, 1997; Ulmer and Stalder, 2001; Akashi et al., 2009; Yoshiasa et al., 2013). HP-CEn is characteristically unquenchable, and will transform to L-CEn at ambient conditions, even on quenching (Angel et al., 1992; Bozhilov et al., 1999; Ulmer and Stalder, 2001). Crystals of HP-CEn have not previously been reported in meteorites, only Bozhilov et al., (1999) inferred that HP-CEn was likely the precursor of the lamellae Clinoenstatite ($P2_1/c$) present in Alpe Arami peridotite (Table 4). In view of the conditions of formation required of HP-CEn, this phase may occur in heavily shocked meteorites.

Our study focuses on the partial transformation of host rock fragments in the shock-induced melt vein of chondrite GRV 022115. The textural characteristics of this meteorite and the identification of the various minerals within the vein were performed utilizing scanning electron microscopy and transmission electron microscopy methods. The combination of these mineralogical characteristics and related forming conditions can enhance knowledge of the possible phase transitions that occurred during intense shock events in early solar system.

2. SAMPLE AND ANALYTICAL TECHNIQUES

GRV 022115 is a chondrite meteorite collected by the Chinese Antarctic Research Expedition Team in 2003, from the Grove Mountain region of Antartica. The sample is curated at the China Polar Research Institute Center (PRIC), and was classified as an L6 S5 chondrite.

Our studies were completed on a polished thin section of the GRV022115 sample, prepared for scanning electron microscope (SEM) observation and electronic probe microanalysis (EPMA). Petrographic characterization, textural observation and back-scattered electron (BSE) imagery were performed on the Scios-FIB emission field SEM, equipped with an Energy Dispersive X-ray Spectrometer (EDS) housed in the Institute of Geochemistry, Chinese Academy of Sciences, Guiyang. The majority of the BSE images were acquired under condition of high vacuum, at 15 kV-accelerating voltage, and a sample-to-objective working distance of ~7 mm.

In situ analyses of the mineral encountered in GRV 022115 and their elemental compositions were completed utilizing the JEOL JXA-8230 electron microprobe at Guilin University of Technology, China. The mineral analyses were carried out with an accelerating voltage (15 kV) and 20 nA beam current. Determination of the minerals present and their compositions in the host rock utilized a focused beam size of 10 μm, whereas for the micron-sized minerals in the meteorites' shock vein analyses were performed with a focused beam size of 1–2 μm. Natural and synthetic minerals were used as standards: Albite (for Al, Na and Si), forsterite (Mg), phlogopite (K), wollastonite (Ca), Ni-oxide (Ni), Mn-oxide (Mn), fayalite (Fe), Cr metal (Cr), rutile (Ti), apatite (P). Corrections were conducted by ZAF procedures.

Focused-ion-beam (FIB) cross sections of the meteorite sample, with a thickness of approximately 100 nm, were prepared by FEI Scios dual-beam methods and characterized using FEI Talos F200X field-emission scanning transmission electron microscope (FE-STEM), operated at 200 kV, at the Guangzhou Institute of Geochemistry and the Suzhou Institute of Nano-tech and Nano-bionics, Chinese Academy of Sciences. Phase identification and their chemical analysis in the FIB cross sections were performed using an X-ray energy-dispersive analyzer equipped on the

STEM instrument. The crystal structures of the newly observed, nano-meter scale phases were confirmed by high resolution (HRTEM) images and selected area electron diffraction (SAED) patterns.

Our estimate for the solidification time of the shock melt vein, within the GRV 022115 meteorite, was done by reference to the model of Turcotte and Schubert (2014). This model has been used previously to constrain the solidification times of shock-induced melt veins in several meteorites (Pang et al., 2016; Baziotis et al., 2018). In our study, the vein was viewed as a thin slab, and the solidification time t_s can be obtained through the following relationship:

$$t_s = \frac{\omega^2}{4\kappa\lambda^2} \quad (1)$$

where ω is the half-width of the slab, κ is the thermal diffusivity, and λ is a dimensionless coefficient. λ can be acquired by the following equation:

$$\frac{L\sqrt{\pi}}{C_p(T_m - T_0)} = \frac{e^{-\lambda^2}}{\lambda(1 + erf\,\lambda)} \quad (2)$$

The values used for the modelling of the GRV 022115 sample were: $L = 320$ kJ kg^{-1}, $C_p = 1.2$ kJ K^{-1} kg^{-1}, $\kappa = 10^{-6}$ m^2 sec^{-1}, $T_m = 1800$ °C and $T_0 = 100$ °C. Our calculations yielded: $\lambda = 0.90$ and $t_s = 112$ ms.

3. RESULTS

3.1. Petrography

The examined thin section of GRV 022115 displayed heavily shocked characteristics, and a network of melt veins that extended across the whole sample. The major minerals in GRV 022115 included olivine (Fa 24), orthopyroxene (Fs 20), and plagioclase (almost completely transformed to optically isotropic maskelynite) (Table 1), with minor amounts of iron-nickel alloy and troilite also present. The homogenization of the major mineral compositions and blurring of chondrule outlines suggest that GRV 022115 is a type 6 ordinary chondrite. Fracture textures are pervasive throughout the olivine and pyroxene grains. A ~1.2 mm wide melt vein is present, extending almost across the whole sample. The vein hosted abundant lithic fragments, ranging in size from several micrometers to 500 μm, embedded in the holocrystalline micron-sized matrix of the vein (Fig. 1A and D). These fragments consist of micrometer-size ringwoodite crystals (Fa 35), silicate

Table 1
Chemical composition of major minerals in both host rock and shock vein within GRV 022115 as determined obtained by EPMA.

	Host rock						Shock vein			
	Olivine (10)		Pyroxene (11)		Maskelynite (7)		Majorite (6)		Ringwoodite	
	Avg	1-σ	Avg	1-σ	Avg	1-σ	Avg	1-σ	1	2
Na_2O	bd	–	bd	–	9.72	0.17	1.63	0.13	bd	bd
SiO_2	38.4	1.05	56.0	0.47	67.8	0.65	55.7	0.79	36.8	36.3
Al_2O_3	0.06	0.12	0.12	0.02	19.2	0.81	0.12	0.03	0.05	0.03
MgO	39.3	1.15	29.3	0.38	0.04	0.02	29.0	0.79	34.1	32.3
K_2O	bd	–	bd	–	0.85	0.09	bd	–	bd	bd
CaO	0.04	0.02	0.83	0.14	1.65	0.11	0.85	0.05	0.06	0.35
P_2O_5	bd	–	bd	–	bd	–	bd	–	bd	bd
NiO	0.15	0.19	0.21	0.17	bd	–	0.12	0.08	0.34	0.35
MnO	bd	–	bd	–	bd	–	bd	–	bd	bd
FeO	22.3	0.32	13.6	0.20	0.46	0.06	12.2	0.96	30.4	32.2
Cr_2O_3	0.60	1.69	0.13	0.04	bd	–	0.13	0.05	bd	bd
TiO_2	0.03	0.02	0.18	0.04	0.06	0.02	0.17	0.04	bd	bd
Total	100.9		100.4		99.8		99.9		101.8	101.5
Formula (O = 24)										
Na	–		–		2.49		0.45		–	–
Si	5.94		7.96		8.94		7.95		5.88	5.87
Al	0.01		0.02		2.99		0.02		0.01	0.01
Mg	9.06		6.20		0.01		6.17		8.12	7.78
K	–		–		0.14		–		–	–
Ca	0.01		0.13		0.23		0.13		0.01	0.06
P	–		–		–		–		–	–
Ni	0.02		0.02		–		0.01		0.04	0.05
Mn	–		–		–		–		–	–
Fe	2.89		1.62		0.05		1.46		4.05	4.35
Cr	0.07		0.01		–		0.02		–	–
Ti	–		0.02		0.01		0.02		–	–
Sum	18.01		16.00		14.87		16.23		18.11	18.11
	Fa 24.2		Fs20.4		Ab 87.1				Fa 33	Fa 35.9

Note. bd = below detection limits.
Avg = average; Fa = fayalite; Fs = ferrosilite; Ab = albite. Number in brackets is the number of EPMA spot analyses performed.
All iron is assumed to be ferrous.

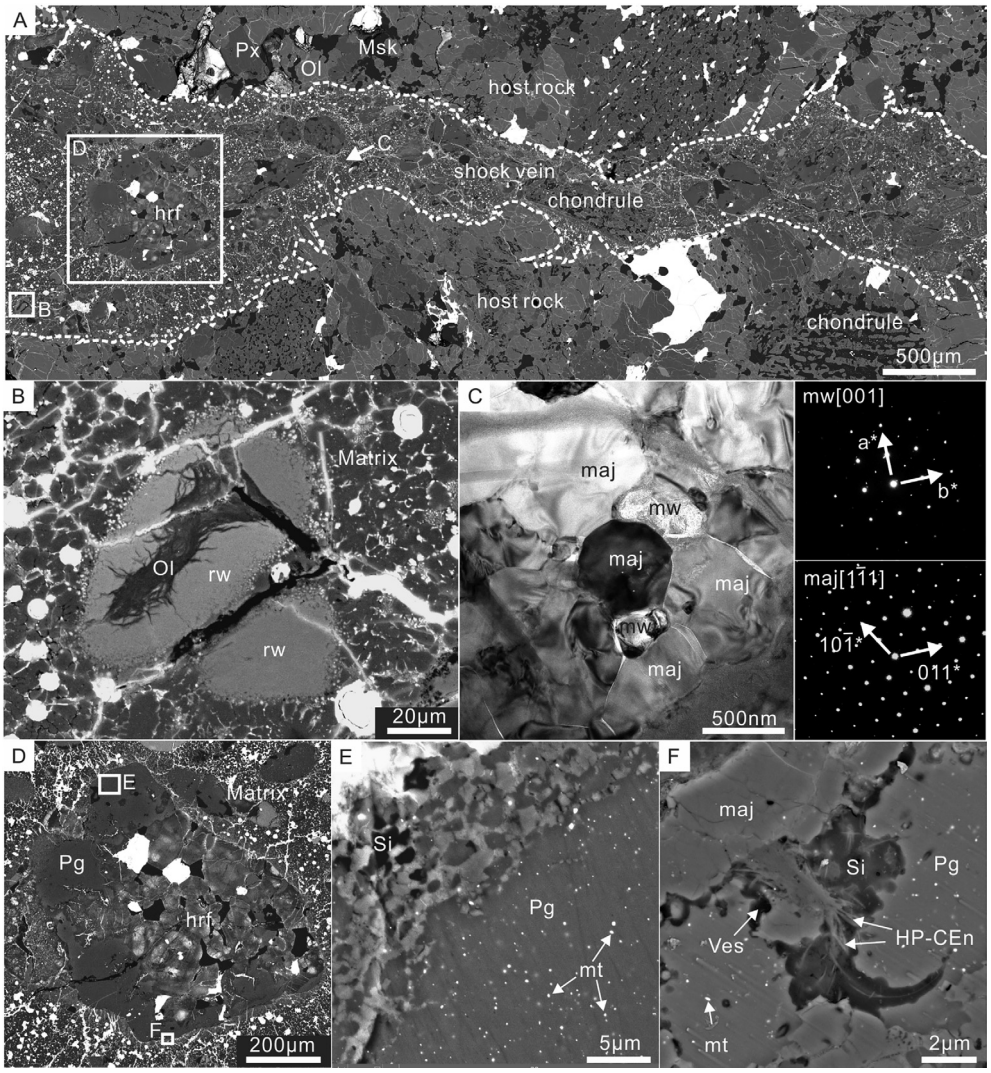

Fig. 1. (A) Back-scattered electron (BSE) image of the ~1.2 mm wide shock melt vein within GRV 022115 studied in this work. White rectangles represent the locations of BSE images (B)-(D). Px: pyroxene; Ol: olivine; Msk: maskelynite. (B) A more detailed view of the interior of the shock view, where olivine (Ol) is partially transformed to ringwoodite (rw), which forms an enclosing rim to the olivine. (C) Bright-field TEM image of the shock vein matrix showing majorite (maj) plus irregularly shaped magnesiowüstite (mw) crystals. The SAED patterns for the [0 0 1] zone axis of magnesiowüstite (upper right) and [1 1 1] zone axis of majorite (lower right) are also presented. (D) BSE image of the studied host rock fragment (hrf), occurring close to the center of melt vein. White rectangles represent the location of (E)–(F). Pg: pyroxene glass. (E) A more detailed BSE image of the pyroxene glass (Pg) found within host rock fragment, abundant nano-sized metal (mt) droplets were embedded in the pyroxene glass. Some silica glass (Si) was also identified at the edge of pyroxene glass. The white rectangle indicates the location of focused ion beam (FIB) cross section. (F) A close up view under BSE imagery of the complex mineral assemblages occurring at the boundary between majorite (maj) and the pyroxene glass (Pg), including the phases: high pressure clinoenstatite (HP-CEn) as acicular crystals, silica glass (Si), nano-phase metal grains (mt), and vesicles (Ves). The white rectangle indicates the location of FIB cross section.

minerals or their high-pressure polymorphs, and a whole chondrule (Fig. 1B). Collectively, these features indicate a shock stage of S5 (Stöffler et al., 1991).

There is single larger (0.5 mm) host rock fragment (hrf) with a sub-rounded shape, in the widest part of the vein (Fig. 1A), this fragment likely originated as a multi-phase chondrule. Under BSE imagery, the petrology of this host rock fragment is that of a large, transformed chondrule (plagioclase + troilite + olivine) that is surrounded by a probable glassy selvage of pyroxene (Fig. 1D), which is the primary focus of our study. Olivine accounts for up to 60 vol.% of the host rock fragment, with a determined Fa value of between ~Fa 29 (rim) and ~Fa 21 (core). Bulk composition of the pyroxene glass within the shocked fragment resembles majorite, and is considered to be transformed from the original pyroxene of the chondrule; the elevated Na_2O content of this pyroxene glass can reconciled with the Na depletion observed in the plagioclase in the host rock fragment (Table 2). Many nano-sized metal droplets were observed, embedded within the pyroxene glass, including iron-nickel metal, iron sulfide and nanophase native iron particles (np-Fe^0); the np-Fe^0 grains were

Table 2
Chemical composition of multiphases in study host rock fragment (hrf) of GRV 022115 as determined by EPMA.

	Center of olivine		Edge of olivine		Pyroxene glass			plagioclase (5)	
	1	2	1	2	1	2	3	Avg	1-σ
Na_2O	0.04	0.02	0.02	0.02	1.87	1.73	1.79	7.48	0.40
SiO_2	38.3	38.3	38.5	36.3	55.8	57.0	54.9	68.6	0.61
Al_2O_3	bd	bd	0.04	bd	0.14	0.17	0.11	18.9	0.53
MgO	42.0	41.6	36.0	35.0	26.7	29.9	27.8	0.35	0.06
K_2O	0.03	bd	0.03	bd	bd	bd	bd	0.48	0.06
CaO	0.04	0.07	0.03	0.04	0.84	0.75	0.66	3.37	0.40
P_2O_5	bd	0.05	0.04	bd	bd	bd	bd	bd	–
NiO	0.17	0.31	bd	0.37	bd	0.08	bd	0.07	0.08
MnO	bd	bd	bd	bd	bd	bd	bd	0.05	0.04
FeO	19.8	20.1	25.9	26.3	14.5	12.8	13.3	0.89	0.10
Cr_2O_3	bd	0.06	bd	bd	0.20	0.11	0.04	bd	–
TiO_2	bd	bd	bd	bd	0.11	0.19	0.18	bd	–
Total	100.4	100.5	100.6	98.0	100.2	102.7	98.8	100.2	
Formula (O = 24)									
Na	0.01	0.01	0.01	0.01	0.52	0.47	0.50	1.90	
Si	5.89	5.89	6.06	5.92	8.02	7.93	7.97	8.98	
Al	–	–	0.01	–	0.02	0.03	0.02	2.92	
Mg	9.63	9.54	8.44	8.50	5.73	6.20	6.01	0.07	
K	0.01	–	0.01	–	–	–	–	0.08	
Ca	0.01	0.01	0.01	0.01	0.13	0.11	0.10	0.47	
P	0.00	0.01	0.01	–	–	–	–	–	
Ni	0.02	0.04	–	0.05	–	0.01	–	0.01	
Mn	–	–	–	–	–	–	–	0.01	
Fe	2.54	2.59	3.41	3.58	1.74	1.49	1.62	0.10	
Cr	–	0.01	–	–	0.02	0.01	0.01	–	
Ti	–	–	–	–	0.01	0.02	0.02	–	
Sum	18.11	18.10	17.93	18.07	16.20	16.27	16.25	14.54	
	Fa 21.1	Fa 21.4	Fa 28.2	Fa 29.8				Ab 77.6	

Note. bd = below detection limits.
Avg = average; Fa = fayalite. Number in brackets is the number of EPMA spot analyses performed.
All iron is assumed to be ferrous.

evidenced by the TEM observations (see Section 3.2 below and Fig. 1E). Finally, it should also be noted that the complex mineral assemblages occur at the boundary between the melt vein matrix and the pyroxene glass, implying both the mineral phases and glass formed as a result of the decomposition of pyroxene (Fig. 1F).

3.2. TEM observations

Cross sections were prepared by Focused Ion Beam (FIB) methods, and derive from the edge of pyroxene glass in the host rock fragment, occurring near to the vein matrix (Fig. 1E and F). Both the observed SAED patterns and recorded EDS analyses confirm that the matrix of the melt vein, at its core mainly consisted of the grains of equant Na, Al-bearing majorite with garnet structure, and those anhedral crystals of magnesiowüstite, infilling in the interstice between the idiomorphic majorite (Fig. 1C, Table 1). Comparison of the compositions of the host rock pyroxene, and the majorite indicates an excess of Na_2O content relative to the pyroxene, while the magnesiowüstite crystals show enrichment in Mg, Fe, and O (Table 2). The Na-enriched majorite plus magnesiowüstite assemblage have roughly an homogeneous grain-size distribution, throughout the melt vein center, indicating that the host rock had encountered sufficient extreme shock conditions and duration for these two minerals to crystallize under high pressure and high temperature (Tomioka and Fujino, 1997; Xie et al., 2006c).

Nanophase iron particles (np-Fe^0) (~50 nm in diameter) were determined in the pyroxene glass using TEM analysis. The TEM X-ray mapping results show that the np-Fe^0 are strongly enriched in an iron element and have little to no S, Ni contents, and the SAED pattern of np-Fe^0 can be indexed by α-Fe (Im3m space group) perfectly (Fig. 2). X-ray EDS analyses of those np-Fe^0 grains show variable amounts of non-siderophile elements (Mg, Si) and a little Ni (<1%) (Table 3). Previous studies of nanophase iron particles within the Tenham meteorite reported a similar composition, whereby this was explained by the presence of minute silicate inclusions that were enclosed in those np-Fe^0 grains, as a result of rapid quenching (Leroux et al., 2000). Since it was not possible to perform individual analyses of these nanophase grains, and the Si/Mg atomic ratios of those np-Fe^0 grains are consistent with the surrounding HP-CEn (Table 3), we suggest the light elements detected as part of the analysis are the result of analytical artefacts.

Elongate HP-CEn crystals were observed to be some 20–50 nm wide and ~100 nm in length, with aspect ratios typically around 3 (Fig. 3), which were identified both in chem-

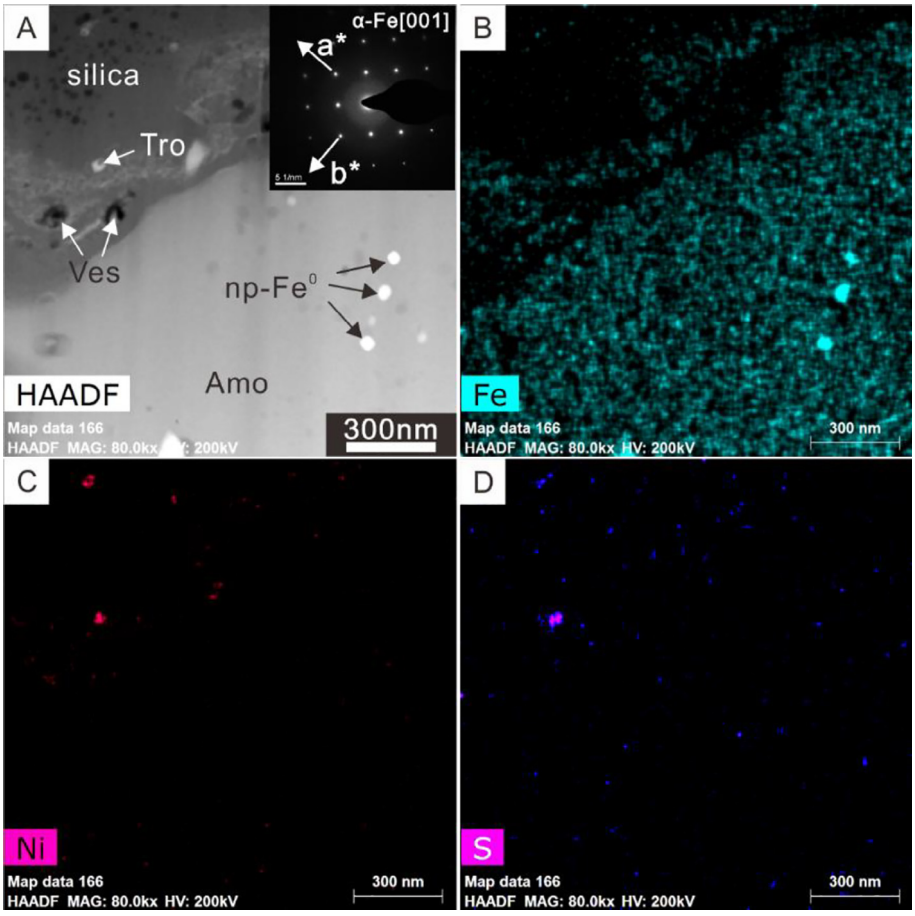

Fig. 2. HAADF image (A) and X-ray element mapping results for Fe (B), Ni (C), and S (D) in the region of FIB cross section (see Fig. 1E) by TEM. The SAED pattern for the [0 0 1] zone axis of α-Fe is inserted at the upper right corner of Fig. 2A. Ves: Vesicles; Tro: troilite; np-Fe^0: nanophase iron particles; Amo: amorphous glass.

Table 3
TEM EDS analyses of various phases in the pyroxene glass of GRV 022115.

	HP-CEn (6)	Amorphous (9)	np-Fe^0 (4)
O=	3	3	
Na	0.01	0.08	0.34
Mg	0.89	0.73	13.72
Si	0.98	1.01	15.24
S	–	–	0.09
Ca	0.01	0.02	0.14
Fe	0.13	0.19	19.77
Ni	–	–	0.19
Total	2.02	2.03	
Fe/(Fe + Mg)	0.13	0.21	
Si/Mg	1.10	1.38	1.11

Note. bd = below detection limits.
Number in brackets is the number of EDS analyses performed.
TEM EDS data has been normalized to 100%.
np-Fe^0 data is the initial measured data (at%).
Fe within HP-CEn and the amorphous glass were assumed to be ferrous.

ical composition and structure by TEM. Quantitative EDS analysis obtained for the HP-CEn nanocrystals and amorphous glass show that both phases have pyroxene stoichiometry, while the iron contents of each phase are lower than that of host rock pyroxene. The enrichments of magnesium and depletions of iron and sodium in HP-CEn, compared with the amorphous glass, suggests chemical diffusion occurred throughout this system during or immediately after the shock conditions (Table 3). HRTEM imagery of the HP-CEn nanocrystals shown along the [0 1 0] zone-axis, record a high density of stacking faults and twin boundaries (Fig. 4A). The (1 0 0) lattice fringes, with a periodicity of 9.24 Å, were determined based on the Fast Fourier Transforms (FFT) from the HRTEM, which is half of the spacing in orthoenstatite (18 Å). Moreover, the [0 1 0] zone-axis FFT patterns lack the reflections with $h = 2n + 1$ suggesting that the structure of HP-CEn is $C2/c$ symmetry (Fig. 4C). Meanwhile, the angle between (0 0 1) and (1 0 0) in FFT pattern measured to be ~82°, beta would be about 98° and roughly consistent with HP-CEn, the HRTEM image also display L-CEn beta angle in unit cell scale, but there are no obviously diffraction spots of L-CEn observed in FFT pattern (see Table 4 for comparison) (Fig. 4A). That observed HRTEM images suggest those nanocrystals are HP-CEn domains and L-CEn domains plus other pyroxene variants (and stacking faults), which could be resulted from fast cooling phase

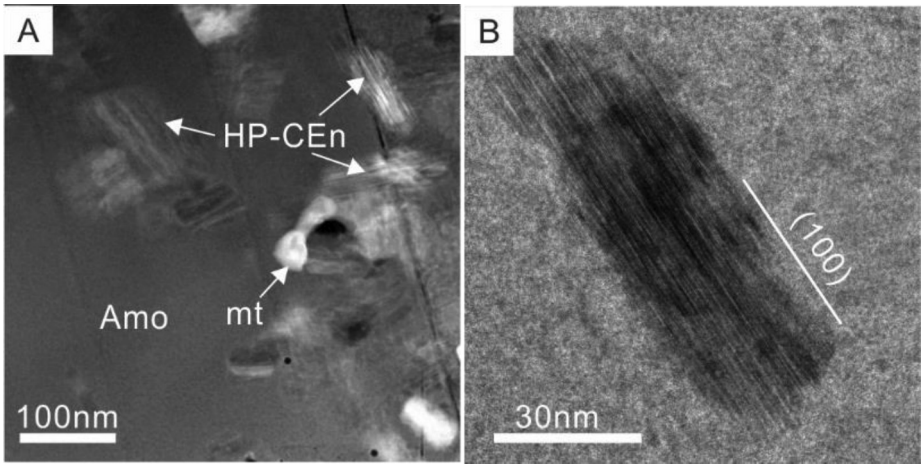

Fig. 3. (A) TEM image of part of the region encompassing the FIB cross section shown in Fig. 1F, highlighting abundant high-pressure clinoenstatite (HP-CEn) nanocrystals associating with nanophase metal (mt) embedded within the amorphous glass (Amo). (B) High-resolution TEM image (HRTEM) of a [0 1 0] zone axis for a single HP-CEn nanocrystal.

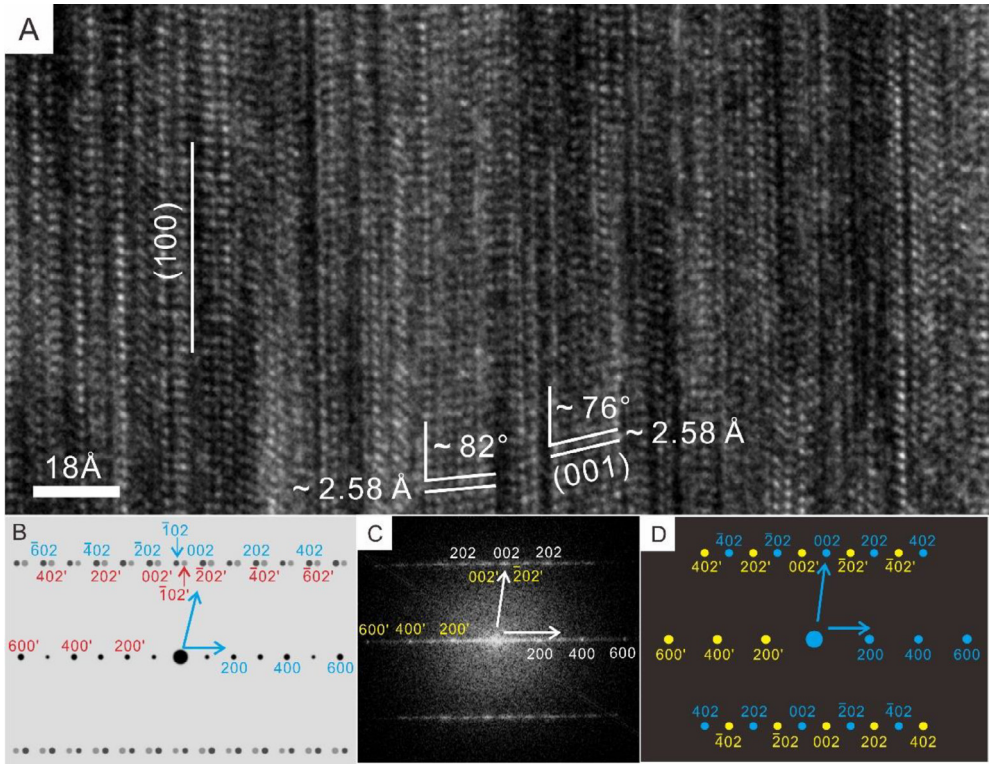

Fig. 4. (A) High-resolution image (HRTEM) of a single high-pressure clinoenstatite (HP-CEn) nanocrystal within pyroxene glass showing (1 0 0) fringes and (0 0 1) fringes with a high density of stacking faults and twinning. (B) The calculated twinned SAED pattern for low clinoenstatite (L-CEn). (C) The [0 1 0] fast Fourier transform (FFT) pattern for the HRTEM image of HP-CEn shown in A. (D) The simulated diffraction patterns of twinned high-pressure clinoenstatite (HP-CEn), and illustrating the same topotaxis as for HP-CEn.

transition (Fig. 4B and D). Considering the tendency of the transformation of majorite to HP-CEn nanocrystals (Fig. 1F), the formation of HP-CEn must have a close relationship to that of the majorite. Furthermore, our analyses show also the presence of pervasive silica glass and vesicles, associating with HP-CEn and np-Fe^0 in the FIB cross sections (Fig. 2A).

4. DISCUSSION

4.1. Constraints on the formation conditions of pyroxene glass

The solid-state transformation of host rock and its included minerals within a shock-induced melt vein is a

Table 4
Unit cell dimensions of the various enstatite polymorphs.

Phase	Space group	a (Å)	b (Å)	c (Å)	β angle (°)
Enstatite (En)[a]	*Pbca*	18.225(1)	8.815(1)	5.175(1)	90
Protoenstatite (PEn)[b]	*Pbcn*	9.252(2)	8.740(1)	5.316(1)	90
Low clinoenstatite (L-CEn)[c]	$P2_1/c$	9.606(1)	8.815(1)	5.169(1)	108.33(1)
High-temperature clinoenstatite (HT-CEn)[d]	$C2/c$	9.5387(8)	8.6601(7)	5.2620(4)	108.701(6)
High-pressure clinoenstatite (HP-CEn)[e]	$C2/c$	9.201(3)	8.621(1)	4.908(1)	101.20(3)

[a] (Ohashi, 1984).
[b] (Murakami et al., 1984).
[c] (Smith, 1969).
[d] (Yoshiasa et al., 2013).
[e] (Angel et al., 1992).

complicated process, as a consequence of the variations in temperature and stress experienced across the rock, the rock competency, the composition and element diffusivities related to each mineral present, and whether or not all original phases are partly or completely transformed (Stöffler et al., 1991; Ohtani et al., 2006; Xie and Sharp, 2007). The presence of ringwoodite in the shock vein provides evidence for the solid-state transformation of olivine at high temperature and high-pressure conditions during shock compression (Chen et al., 1996; Sharp et al., 2006). Studies have observed that olivine transforms to ringwoodite only above 900 °C at ~20 GPa in static high-pressure kinetic experiments (Kerschhofer et al., 2000).

The occurrence of both majorite (Fs 20) and magnesiowüstite as a high pressure mineral assemblage within the melt vein matrix of GRV 022115 indicates melt vein equilibrium shock conditions were in excess of 1800 °C and at 20–23 GPa (Chen et al., 1996; Xie et al., 2006a). We estimate a complete solidification time of the melt vein on the order of 112 ms. This calculation assumes double-sided cooling of a 1200 μm-wide slab of melt from a constrained temperature of ~1800 °C while surrounded by cooler host rock (~100 °C). Hence, the sufficient duration of shock pressure (>112 ms) is required to form a 1.2 mm-wide vein of pervasive majorite that crystallized from the melt under high pressure conditions.

When compared with the ringwoodite (Fa 35) in the melt vein, the morphology and composition of olivine (Fa 29 at the edge and Fa 21 in the core) occurring in the studied host rock fragment, demonstrates that this host rock fragment did not reach sufficient highly temperatures (≈900 °C) to allow for the complete olivine to ringwoodite transformation, during the shock process that affected GRV 022115 (or its parent meteoroid).

From the above evidence and discussion, the studied host rock fragment plays the role of a cold source in the development of the GRV 022115 melt vein, during the process of shock. Since the cooling of the melt vein was predominantly produced by thermal conduction with its surroundings (Langenhorst and Poirier, 2000; DeCarli et al., 2002; Sharp and DeCarli, 2006; Xie et al., 2006b), the pyroxene glass selvage that surrounds the host rock fragment was derived from the cold source (rock fragment); its irregular shape could not form by a process of vitrification after pressure release of the high-pressure polymorph (Price et al., 1979). In the melt vein, the pyroxene glass composition is consistent to that of majorite with an elevated Na_2O content, indicating that the pyroxene glass most likely quenched rapidly from melt instead of having crystallized in equilibrium during decompression (Sharma and Sikka, 1996); hence, the time for pyroxene glass formation should be much less than 112 ms after the shock effect. Meanwhile, there will be shear stresses present between the fragments undergoing solid-state changes and any melt within the vein, as the result of shock compression, and these structural changes may have resulted in extreme heating of the pyroxene precursor through friction to temperatures sufficient to induce melting.

4.2. Formation of np-Fe^0 and HP-CEn

Both HP-CEn and np-Fe^0 are demonstrated products of quenching (Angel et al., 1992; Ulmer and Stalder, 2001; van de Moortele et al., 2007; Akashi et al., 2009). For this reason, extremely rapid cooling offers the possibility for the preservation of HP-CEn and np-Fe^0 within a rock undergoing shock event. Compared with its high pressure polymorph, HP-CEn ($C2/c$), the low clinoenstatite [L-CEn ($P2_1/c$)] is more pervasively observed in terrestrial sample and shocked meteorites (Angel et al., 1992; Price et al., 1979; Tomioka and Miyahara, 2017). Importantly, the HP-CEn phase transformation has been postulated to account for the observed "X"-discontinuity in the Earth's upper mantle, whilst the stability field of HP-CEn was confirmed in many previous studies (Angel et al., 1992; Woodland, 1998; Shinmei et al., 1999; Akashi et al., 2009). In our study, the HP-CEn crystals' (1 0 0) spacing (~9 Å) and the presence of twinning suggest that this phase did not directly form from orthoenstatite (18 Å) (Buseck, 1980). While the (1 0 0) high density stacking faults in HP-CEn crystals can be expected to have formed by a martensitic mechanism (Putnis and Price, 1979), the observation of HP-CEn crystals with other pyroxene variants, and the phase transformation between majorite (garnet phase) and HP-CEn (Fig. 1F) implies that the HP-CEn is the reversion product of majorite, on pressure release. Microcrystalline clinopyroxene ($P2_1/c$) has been interpreted as a reversion product of majorite in studies of the Tenham meteorite (Price et al., 1979). In such a shock case, the pressure releases more rapidly than temperature due to the poor

conductivity of rock (Sharp et al., 2006), so that the HP-CEn nanocrystals in the pyroxene glass were reversed from majorite immediately following pressure release of the shock event, and the formation conditions of HP-CEn should be ~1800 °C at relatively high pressure (<20 GPa). Further, the PEn and Opx domains observed at the unit cell scale in the HP-CEn crystals were interpreted as a local inversion product of HP-CEn. For the previous studies and our observation, HP-CEn does not rapidly transform into Opx during fast cooling process because the transition into Opx is reconstructive type involving breaking strong bonds, needing rearrange of the chain structure and changing stacking sequence (Yoshiasa et al., 2013). HP-CEn had been proved to transform to L-CEn at ambient condition, even on quenching, and L-CEn is pervasively observed in the natural samples (Tomioka and Fujino, 1997; Angel et al., 1992; Ulmer and Stalder, 2001). In the case of pressure and temperature quenching, our result shows that metastable HP-CEn can be frozen and most likely spontaneously transform to L-CEn during quenching, and we speculate that there will have a metastable boundary between HP-CEn and L-CEn in the enstatite phase diagram to convert HP-CEn to L-CEn directly in quenching process (Fig. 5).

For molten systems, smaller metal particles will coalesce with each other as they try to attain decreasing surface energy (Rubie et al., 2015). The occurrence of the np-Fe^0 in pyroxene glass of GRV 022115 is the result of immiscible migration of elemental Fe (Ruzicka et al., 2005) under quenching conditions.

4.3. Decomposition of pyroxene

The presence of nano-sized grains of HP-CEn and np-Fe^0 associated with silica glass and vesicles has been determined, in the pyroxene glass selvage within the GRV 022115 meteorite, by TEM. Based upon their similar composition, and the distribution of elements both in amorphous glass and HP-CEn, we propose that their formation is linked to the decomposition of pyroxene from the fragment of rock, hosted with the melt vein. Compared to the amorphous glass, the quantitative EDS analysis data for HP-CEn displays an enrichment in Mg, as well as depletion in Fe and Na contents. The process of quenching is considered not to be one of chemical equilibrium, as such we can only explain these elemental differences by chemical diffusion of Fe, Mg and Na through the pyroxene glass. Magnesium should preferentially partition into the HP-CEn phase while Fe favours that of the pyroxene glass. Sodium mostly likely was partitioned into the glass because of its large ionic radius that limits its incorporation into the crystal lattice (Chen et al., 2003). When compared to the composition of the host rock pyroxene, we found the Fe/(Mg + Fe) ratios of both amorphous glass and HP-CEn to be lower, which provides a material basis for the formation of np-Fe^0 during pyroxene breakdown. According to the observed element distribution and previous studies, vesicles are considered as evidence for the liberation of O_2, so the emergence of these vesicles provides a potential redox condition attending np-Fe^0 formation. Because the O_2 is very reactive, the formation of vesicles could be contributed to the O_2 or its reaction products. The presence of silica glass also provides support for the decomposition of pyroxene as the result of the shock process. A reaction to explain the formation of the observed assemblage can be written as:

$$FeSiO_3 \rightarrow Fe + SiO_2 + 1/2O_2 \uparrow (MgSiO_3 \text{ remain in the HP-CEn})$$

A similar equation has been reported by Benzerara et al. (2002) in their studies of shock condition affecting the Tatahouine achondrite; here we provide evidence to support the present of native Fe within the pyroxene glass.

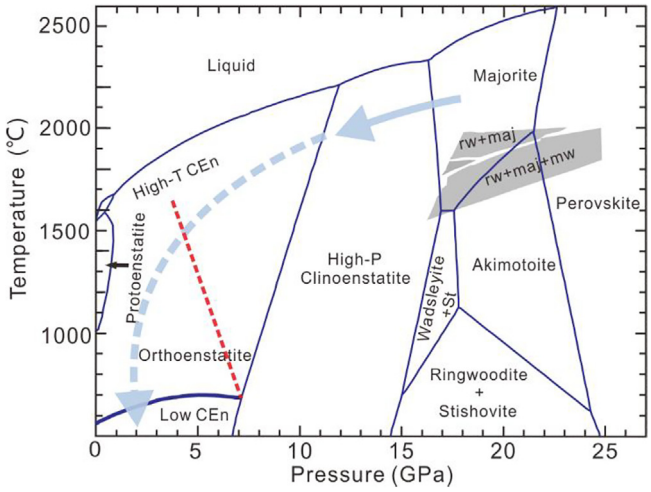

Fig. 5. The crystallization-pressure stability regions for high-pressure minerals pertinent to this study (grey regions), and illustrated on the Temperature-Pressure phase diagram for the $MgSiO_3$ system (Agee et al., 1995; Chen et al., 1996; Gasparik, 2014; Tomioka and Miyahara, 2017; Xie et al., 2006b). The predicted quenching route of HP-CEn is shown by the blue shaded solid arrow, and then it may be converted to L-CEn (blue shaded dotted arrow), the red dotted line represents presumed metastable boundary between HP-CEn and L-CEn. maj: majorite; mw: magnesiowüstite; and rw: ringwoodite. (For interpretation of the references to color in this figure legend, the reader is referred to the web version of this article.)

The Earth owes its origin and evolution to having undergone multiple collisions between proto-planets that inhabited the early Solar System, including one or more very large impacts, during and soon after its initial accretion (Wetherill, 1985). Such dynamic impacts can provide a major source of energy needed to melt rock during the formation of both the planet's core, and likely an important role in subsequent planetary differentiation (Leroux et al., 2000). As impacts dominated the early evolution of the terrestrial planets, these processes could be occurred frequently within the early Solar System, and likely have a great significance to understanding the evolution of matter. There are many studies that provide evidence for iron production by olivine decomposition. Here we present evidence to support the formation of native iron through the breakdown of pyroxene, in response to shock events as those found in our study of the GRV 022115 meteorite. It is plausible to invoke similar conditions having affected the space weathering on airless bodies, the co-reduction of pyroxene and olivine in the ordinary chondrites to produce np-Fe^0 significantly affected the spectral characteristics of S-type asteroids (e.g. Itokawa, Chapman, 2004; Noguchi et al., 2011).

In view of its potential importance to the formation of the Earth, it is fitting to note that the orthorhombic to high-pressure monoclinic phase transition in Mg-Fe pyroxenes has been proposed as a cause of seismic discontinuity in Earth's upper mantle ("X"-discontinuity, Angel et al., 1992; Woodland 1998). Significant differences in cooling rates and equilibrium conditions between deep-Earth and shocked meteorites prevent such observations from being simply invoked in deep-Earth petrology. Our results show that HP-CEn could be quenched metastably in such shocked veins, and the presence of HP-CEn could be regarded as an indicator of quenching condition, which also preserves the metastable phase transitions history record.

Declaration of Competing Interest

The authors declare that they have no known competing financial interests or personal relationships that could have appeared to influence the work reported in this paper.

ACKNOWLEDGMENTS

We thank Jiaxin Si, Hisayoshi Yurimoto for their suggestions and constructive revisions that improved the quality of this manuscript. We would like to appreciate editors and two reviewers for their constructive comments that help us to greatly improved this manuscript. This work was financially supported by the Key Research Program of the Chinese Academy of Sciences, Grant NO. XDPB11 and XDA 15020300, National Natural Science Foundation of China (41673071, 41931077, 41272057).

APPENDIX A. SUPPLEMENTARY MATERIAL

Supplementary data to this article can be found online at https://doi.org/10.1016/j.gca.2019.10.036.

REFERENCES

Agee C. B., Li J., Shannon M. C. and Circone S. (1995) Pressure-temperature phase-diagram for the allende meteorite. *J. Geophys. Res.-Sol. Ea* **100**, 17725–17740.

Akashi A., Nishihara Y., Takahashi E., Nakajima Y., Tange Y. and Funakoshi K. (2009) Orthoenstatite/clinoenstatite phase transformation in $MgSiO_3$ at high-pressure and high-temperature determined by in situ X-ray diffraction: Implications for nature of the X discontinuity. *J. Geophys. Res.-Sol. Ea*, 114.

Angel R. J., Chopelas A. and Ross N. L. (1992) Stability of high-density clinoenstatite at upper-mantle pressures. *Nature* **358**, 322–324.

Barrat J. A., Yamaguchi A., Jambon A., Bollinger C. and Boudouma O. (2012) Low-Mg rock debris in howardites: evidence for KREEPy lithologies on Vesta?. *Geochim. Cosmochim. Acta* **99** 193–205.

Baziotis I., Asimow P. D., Hu J., Ferriere L., Ma C., Cernok A., Anand M. and Topa D. (2018) High pressure minerals in the Chateau-Renard (L6) ordinary chondrite: implications for collisions on its parent body. *Sci. Rep.* **8**, 9851.

Benzerara K., Guyot F., Barrat J. A., Gillet P. and Lesourd M. (2002) Cristobalite inclusions in the Tatahouine achondrite: implications for shock conditions. *Am. Mineral.* **87**, 1250–1256.

Bläß U. W., Langenhorst F. and McCammon C. (2010) Microstructural investigations on strongly stained olivines of the chassignite NWA 2737 and implications for its shock history. *Earth Planet. Sci. Lett.* **300**(3–4), 255–263.

Boland J. N. and Duba A. (1981) Solid-State reduction of iron in olivine - planetary and meteoritic evolution. *Nature* **294**, 142–144.

Bozhilov K. N., Green H. W. and Dobrzhinetskaya L. (1999) Clinoenstatite in Alpe Arami peridotite: additional evidence of very high pressure. *Science* **284**, 128–132.

Buseck P. R., Nord, Jr., G. L. and Veblen D. R. (1980) Subsolidus phenomena in pyroxenes. *Rev. Mineral. Geochem.* **7**, 117–211.

Chapman Clark R. (2004) Space weathering of asteroid surfaces. *Ann. Rev. Earth Planet. Sci.* **32**(1), 539–567.

Chen M., Sharp T. G., ElGoresy A., Wopenka B. and Xie X. D. (1996) The majorite-pyrope plus magnesiowustite assemblage: constraints on the history of shock veins in chondrites. *Science* **271**, 1570–1573.

Chen M., Xie X. and Goresy A. E. (2003) Geochemical behavior of alkaline elements in the deep earth: evidence from high-pressure minerals in shocked meteorites. *Geochimica* **32**, 161–166.

DeCarli P. S., Bowden E., Sharp T. G., Jones A. P. and Price G. D. (2002) Evidence for kinetic effects on shock wave propagation in tectosilicates. *AIP Conf. Proc.* **620**, 1381–1384.

Frost D. J., Liebske C., Langenhorst F., Mccammon C. A., Trønnes R. G. and Rubie D. C. (2004) Experimental evidence for the existence of iron-rich metal in the earth's lower mantle. *Nature* **428**(6981), 409–412.

Gasparik T. (2014) *Phase Diagrams for Geoscientists: An Atlas of Earth's Interior*. Springer, pp. 13–24.

Kerschhofer L., Rubie D. C., Sharp T. G., McConnell J. D. C. and Dupas-Bruzek C. (2000) Kinetics of intracrystalline olivine-ringwoodite transformation. *Phys. Earth Planet. Inter.* **121**, 59–76.

Langenhorst F. and Poirier J. P. (2000) Anatomy of black veins in Zagami: clues to the formation of high-pressure phases. *Earth Planet. Sci. Lett.* **184**, 37–55.

Lappe S. C. L. L., Church N. S., Kasama T., Fanta A. B. D., Bromiley G., Dunin-Borkowski R. E., Feinberg J. M., Russell S. and Harrison R. J. (2011) Mineral magnetism of dusty olivine: a credible recorder of pre-accretionary remanence. *Geochem Geophy Geosy* **12**.

Leroux H., Doukhan J. C. and Guyot F. (2000) Metal-silicate interaction in quenched shock-induced melt of the Tenham L6-chondrite. *Earth Planet. Sci. Lett.* **179**, 477–487.

Leroux H., Libourel G., Lemelle L. and Guyot F. (2003) Experimental study and TEM characterization of dusty olivines in chondrites: evidence for formation by in situ reduction. *Meteorit. Planet. Sci.* **38**, 81–94.

Murakami T., Takeuchi Y. and Yamanaka T. (1984) X-ray studies on protoenstatite. 2. Effect of temperature on the structure up to near the incongruent melting-point. *Z. Kristallogr.* **166**, 263–275.

Noguchi T., Nakamura T., Kimura M., Zolensky M. E., Tanaka M., Hashimoto T., Konno M., Nakato A., Ogami T., Fujimura A., Abe M., Yada T., Mukai T., Ueno M., Okada T., Shirai K., Ishibashi Y. and Okazaki R. (2011) Incipient space weathering observed on the surface of Itokawa dust particles. *Science* **333**, 1121–1125.

Ohashi Y. (1984) Polysynthetically-twinned structures of enstatite and wollastonite. *Phys. Chem. Miner.* **10**, 217–229.

Ohtani E., Kimura Y., Kimura M., Kubo T. and Takata T. (2006) High-pressure minerals in shocked L6-chondrites: constraints on impact conditions. *Shock Waves* **16**, 45–52.

Palme H., Wlotzka F., Spettel B., Dreibus G. and Weber H. (1988) Camel Donga - a Eucrite with high metal content. *Meteoritics* **23**, 49–57.

Pang R. L., Zhang A. C., Wang S. Z., Wang R. C. and Yurimoto H. (2016) High-pressure minerals in eucrite suggest a small source crater on Vesta. *Sci. Rep.* **6**, 26063.

Price G. D., Putnis A. and Agrell S. O. (1979) Electron petrography of shock-produced veins in the tenham chondrite. *Contrib. Mineral. Petrol.* **71**, 211–218.

Putnis A. and Price G. D. (1979) High-pressure (Mg, Fe) $_2SiO_4$ phases in the tenham chondritic meteorite. *Nature* **280**, 217–218.

Robertson P. B., Grieve R. A. F., Pepin R. O. and Merrill R. B. (1977) Shock attenuation at terrestrial impact structures. *Impact Explos. Crater.: Planet. Terr. Implicat.*.

Rubie D. C., Nimmo F. and Melosh H. J. (2015) *Formation of the Earth's Core*. Elsevier, pp. 43–79.

Ruzicka A., Killgore M., Mittlefehldt D. W. and Fries M. D. (2005) Portales valley: petrology of a metallic-melt meteorite breccia. *Meteorit. Planet. Sci.* **40**, 261–295.

Sasaki S., Nakamura K., Hamabe Y., Kurahashi E. and Hiroi T. (2001) Production of iron nanoparticles by laser irradiation in a simulation of lunar-like space weathering. *Nature* **410**, 555–557.

Sharma S. M. and Sikka S. K. (1996) Pressure induced amorphization of materials. *Prog. Mater. Sci.* **40**, 1–77.

Sharp T. G. and DeCarli P. S. (2006) *Shock effects in meteorites. Meteorites and the Early Solar System II*. University of Arizona Press, pp. 653–677.

Shinmei T., Tomioka N., Fujino K., Kuroda K. and Irifune T. (1999) In situ X-ray diffraction study of enstatite up to 12 GPa and 1473 K and equations of state. *Am. Mineral.* **84**, 1588–1594.

Smith J. V. (1969) Magnesium pyroxenes at high temperature - inversion in clinoenstatite. *Nature* **222**, 256.

Stöffler D., Keil K. and Edward R. D. S. (1991) Shock metamorphism of ordinary chondrites. *Geochim. Cosmochim. Acta* **55**, 3845–3867.

Stoffler D. and Langenhorst F. (1994) Shock metamorphism of quartz in nature and experiment. 1. Basic observation and theory. *Meteoritics* **29**, 155–181.

Tomioka N. and Fujino K. (1997) Natural (Mg, Fe) SiO_3-ilmenite and -perovskite in the Tenham meteorite. *Science* **277**, 1084–1086.

Tomioka N. and Miyahara M. (2017) High-pressure minerals in shocked meteorites. *Meteorit. Planet. Sci.* **52**, 2017–2039.

Turcotte D. L. S. and Schubert G. (2014) *Geodynamics*, third ed. Cambridge University Press.

Ulmer P. and Stalder R. (2001) The Mg (Fe) SiO_3 orthoenstatite-clinoenstatite transitions at high pressures and temperatures determined by Raman-spectroscopy on quenched samples. *Am. Mineral.* **86**, 1267–1274.

van de Moortele B., Reynard B., Rochette P., Jackson M., Beck P., Gillet P., McMillan P. F. and McCammon C. A. (2007) Shock-induced metallic iron nanoparticles in olivine-rich Martian meteorites. *Earth Planet. Sci. Lett.* **262**, 37–49.

Warren P. H., Rubin A. E., Isa J., Gessler N., Ahn I. and Choi B. G. (2014) Northwest Africa 5738: Multistage fluid-driven secondary alteration in an extraordinarily evolved eucrite. *Geochim. Cosmochim. Acta* **141**, 199–227.

Wetherill G. W. (1985) Occurrence of giant impacts during the growth of the terrestrial planets. *Science* **228**(4701), 877–879.

Woodland A. B. (1998) The orthorhombic to high-P monoclinic phase transition in Mg-Fe pyroxenes: can it produce a seismic discontinuity? *Geophys. Res. Lett.* **25**, 1241–1244.

Xie X. D., Chen M. and Wang D. Q. (2006a) High-pressure mineral assemblages in shock melt veins of Suizhou meteorite. *Meteorit. Planet. Sci.* **41**. A191–A191.

Xie Z. D., Sharp T. G. and De Carli P. S. (2006b) Estimating shock pressures based on high-pressure minerals in shock-induced melt veins of L chondrites. *Meteorit. Planet. Sci.* **41**, 1883–1898.

Xie Z. D., Sharp T. G. and DeCarli P. S. (2006c) High-pressure phases in a shock-induced melt vein of the Tenham L6 chondrite: constraints on shock pressure and duration. *Geochim. Cosmochim. Acta* **70**, 504–515.

Xie Z. D. and Sharp T. G. (2007) Host rock solid-state transformation in a shock-induced melt vein of Tenham L6 chondrite. *Earth Planet. Sci. Lett.* **254**, 433–445.

Xu H. F., Hill T. R., Konishi H. and Farfan G. (2017) Protoenstatite: A new mineral in Oregon sunstones with "watermelon" colors. *Am. Mineral.* **102**, 2146–2149.

Yoshiasa A., Nakatsuka A., Okube M. and Katsura T. (2013) Single-crystal metastable high-temperature *C*2/*c* clinoenstatite quenched rapidly from high temperature and high pressure. *Acta Crystallogr. B* **69**, 541–546.

Associate Editor: Christian Koeberl